Journal of Materials Chemistry A

ROYAL SOCIETY OF CHEMISTRY

PAPER

View Article Online
View Journal

Check for updates

Cite this: DOI: 10.1039/d5ta07993d

Influence of current collector materials on the electrochemical performance of aqueous zinc-ion batteries

Iman P. Pinnock,[a] Yujia Fan,[a] Ivan P. Parkin *[b] and Buddha Deka Boruah *[a]

Aqueous zinc-ion batteries (ZIBs) have recently attracted increasing attention due to their intrinsic advantages, including high safety, the natural abundance of zinc, cost-effectiveness, and a reduced environmental footprint. However, ZIBs are still in the early stages of development for practical applications. Current research is focused on designing high-capacity cathodes, dendrite-free Zn anodes, and optimised electrolytes and separators. While much emphasis has been placed on electrode materials, the role of cathode current collectors is equally critical, as they support the cathode material and facilitate electron transport. The choice of current collector significantly influences the electrical, mechanical, and electrochemical performance of the battery. It serves as both the structural backbone for the active material and a conduit for efficient charge transfer, helping to minimise resistance and voltage losses. In this study, we investigate six different materials – carbon paper, graphene paper, carbon nanotube paper, titanium foil, stainless steel foil, and stainless-steel mesh – as cathode current collectors for ZIBs. Remarkably, batteries employing graphene paper and carbon paper current collectors demonstrate high specific capacities of 407 and 429 mAh g^{-1}, respectively, at a high specific current of 2000 mA g^{-1}. In contrast, AZIBs using titanium foil and stainless-steel foil exhibit significantly lower capacities of 280 and 172 mAh g^{-1}, respectively. These findings underscore the critical role of current collector material and highlight carbon-based collectors as promising candidates for high-performance ZIBs, even when using the same VO_2(B) cathode material.

Received 29th September 2025
Accepted 24th April 2026

DOI: 10.1039/d5ta07993d

rsc.li/materials-a

Open Access Article. Published on 24 April 2026. Downloaded on 6/4/2026 6:31:48 PM.
This article is licensed under a Creative Commons Attribution-NonCommercial 3.0 Unported Licence.

Introduction

The increasing demand for alternative energy sources, driven by the depletion of non-renewable resources, has intensified the focus on battery technologies.[1] Among these, lithium-ion batteries (LIBs) currently dominate due to their high energy densities and long-term cycling stability. However, despite these advantages, LIBs face several drawbacks, including high production costs, limited stability, electrolyte issues, and safety concerns.[2,3] In applications where cost and safety are critical – such as mini off-grid systems – alternative battery technologies are essential. Zinc-ion batteries (ZIBs) have emerged as promising candidates due to their inherent benefits: zinc (Zn) is abundant and inexpensive, offers high ambient stability, and supports easy fabrication processes.[4,5] Additionally, Zn metal anodes are attractive because of their high theoretical gravimetric (820 mAh g^{-1}) and volumetric (5855 mAh cm^{-3}) capacities, and their compatibility with aqueous electrolytes, which increases safety,[6] thanks to a low redox potential of −0.76 V *vs.* SHE (standard hydrogen electrode). They are a promising, green alternative to the commercial LIB.[7] For cathodes, oxide-based materials such as vanadium-based, manganese-based, or Prussian blue analogues are commonly used, due to their structures stability and multivalent states allowing the facilitation (de) intercalation of bivalent zinc ions.[8]

Manganese based cathode materials yield a high theoretical specific capacity (309 mAh g^{-1}),[9] affordability, and environmental safeness and friendlessness.[10] Polyvalent manganese oxides have multiple crystal structures, providing frameworks to accommodate various ions.[10,11] However, severe capacity fading is exhibited during the dissolution of manganese.[11] Prussian blue analogues' open framework structure,[10,12] coupled with a centred cubic lattice, results in large ion-intercalation sites.[8] However, the theoretical capacity is lower than that of manganese based materials (120 and 100 mAh g^{-1}),[8,12] and though the large interstitial sites easily allow reversible electrochemical insertion/extraction of ions,[13] this capacity makes it unattractive. Vanadium based materials (especially oxides) possess a large tunnel like framework suitable for ion intercalation. Vanadium pentoxide has covalent and hydrogen bonds, and weak van der Waal forces, permitting Zn^{2+} to attach/detach freely;[8] however it is subject to instability and low capacity when cycled repeatedly due to the unstable single layer structure of the material, and the +5 valence.[14,15] Vanadium dioxide (VO_2) has many polymorphs with unique, complex

[a]Institute for Materials Discovery (IMD), University College London (UCL), London WC1E 7JE, UK. E-mail: b.boruah@ucl.ac.uk
[b]Department of Chemistry, University College London (UCL), London WC1H 0AJ, UK. E-mail: i.p.parkin@ucl.ac.uk

Open Access Article. Published on 24 April 2026. Downloaded on 6/4/2026 6:31:48 PM. This article is licensed under a Creative Commons Attribution-NonCommercial 3.0 Unported Licence.

crystal frameworks, however VO_2(B) has a distinct structure composed of edge sharing, distorted VO_6 octahedra, which can withstand repeated (de)intercalation of ions.[9,10] In addition, the theoretical specific capacity of VO_2(B) is 323 mAh g^{-1}, which is higher than that of manganese-based materials.[16]

Despite their promise, ZIBs are still in the early stages of development and face several challenges, including Zn dendrite formation, cathode dissolution, and gradual capacity fading.[8,17] To overcome these issues, current research focuses on advancing various battery components – electrolytes,[18] cathode and anode materials,[19,20] and separators[21] – all of which play key roles in improving battery performance. Additionally, optimising binders and incorporating functional additives is being explored to enhance battery functionality by improving reversibility,[22] minimising dendrite formation,[23] and reinforcing structural integrity.[24,25]

On the other hand, among the essential components of ZIBs, the current collectors (CCs) also play a vital role, particularly for cathode materials. Since Zn foil can be directly used as the anode in ZIBs, the design and performance of the cathode current collector become especially critical. The cathode CC serves to conduct and channel electrons between the active material and the external circuit, enabling continuous electron flow during operation.[26] During charge and discharge processes, the CC collects the current generated by the movement of electrons between the active materials of the cathode and anode.[27] In addition to their conductive role, CCs also physically support the electrode material, which is typically casted, sprayed, or coated as a slurry onto the CC for enhanced structural stability.[28–31] By serving as the physical backbone for the electrode, CCs help ensure uniform distribution of active materials and efficient charge/discharge transfer. To facilitate this electron transfer, consistent and intimate contact between the CC and the electrode material must be maintained throughout cycling.[32] Furthermore, the internal structure of the electrode should support effective electron transport from the active materials to the CC and eventually to the external circuit. Typically, cathodes are composed of active material, a conductive additive, and a binder. Despite their significance, studies investigating the suitability of current collectors for ZIBs remain limited, and identifying optimal materials is still an open challenge.

In this study, we investigated a range of CCs for ZIB cathodes, including carbon paper, graphene paper, carbon nanotube (CNT) paper, titanium foil, stainless steel foil, and stainless-steel mesh. These CCs were paired with VO_2(B) cathode materials, and a series of sequential electrochemical studies were conducted to evaluate their impact on ZIB performance. The findings contribute to a deeper understanding of suitable CCs for enhancing the electrochemical performance of ZIBs.

Experimental section

Chemicals

The raw materials used for synthesising VO_2(B) were vanadium(v) oxide (V_2O_5, Sigma-Aldrich) and oxalic acid dihydrate ($H_2C_2O_4 \cdot 2H_2O$, Scientific Laboratory Supplies). For slurry preparation, the following materials were used: Super P conductive carbon black (MTI Corporation), polyvinylidene fluoride (PVDF, Alfa Aesar), and *N*-methyl-2-pyrrolidone (NMP, Sigma-Aldrich). All chemicals were used as received without further purification.

Material synthesis

VO_2(B) was synthesised *via* a hydrothermal method.[33] V_2O_5 (3.0 g) and $H_2C_2O_4 \cdot 2H_2O$ (4.5 g) were mixed with 100 mL of deionised water and stirred magnetically at 75 °C for 1 hour. The solution was transferred into a 150 mL Teflon-lined stainless-steel autoclave and heated at 180 °C for 72 hours. After cooling, the product was washed three times alternately with deionised water and ethanol *via* centrifugation and then dried under vacuum at 70 °C overnight.

Material characterisation

X-ray diffraction (XRD) was performed using a PANalytical AERIS benchtop XRD system to investigate the crystal structure of the synthesised VO_2(B). Raman spectroscopy (Renishaw inVia Raman microscope) was used to confirm the chemical structure, phase, and polymorphism. Scanning electron microscopy (SEM) was conducted using a Zeiss EVO LS15 to examine the morphology of the material.

Cathode fabrication

Cathodes were prepared using VO_2(B) as the active material with a range of CCs: carbon paper, graphene paper, CNT paper, titanium foil, stainless steel (SS) foil, and stainless-steel mesh. The cathode slurry consisted of VO_2(B), Super P, and PVDF in a 7 : 2 : 1 mass ratio. To ensure uniform dispersion, PVDF was first dissolved in NMP at 80 °C under stirring. VO_2 and Super P were pre-mixed in a Thinky mixer for 3 cycles of 2 minutes each. Additional NMP was incrementally added for viscosity adjustment. After adding the PVDF solution, the slurry was further mixed in three cycles. The prepared slurry was cast onto the CCs using a doctor blade set to 150 μm thickness and dried on a hotplate at 50 °C for 60 minutes (depending on thickness). The coated electrodes were then dried under vacuum at 70 °C for 12 hours. The active material loading accounted for 70% of the total dried slurry mass. The active material mass loading of the cathodes was between 2.4 and 3.5 mg cm^{-2}, which was chosen as it is the standard mass loading where cracking is minimal – when mass loading is increased, cracking becomes the prevalent issue, disrupting interfacial contact and cell performance, however it has been seen in other studies that an increase in mass loading results in an increase in capacity until a certain point.[31] The masses of each CC materials are; 7.7 mg cm^{-2} for carbon paper, 7.3 mg cm^{-2} for graphene paper, 1.37 mg cm^{-2} for CNT paper, 22.0 mg cm^{-2} for titanium foil, 23.3 mg cm^{-2} for stainless steel foil and 15.0 mg cm^{-2} for stainless steel mesh (it is lower than the foil does to the wholes within the mesh). To ensure uniformity in the surface density of the active substances on the current collector the slurry was mixed thoroughly at each stage and made as a large batch so that the same slurry was casted on all the different current collector materials. A doctor blade with a certain thickness was

 This journal is © The Royal Society of Chemistry 2026

Open Access Article. Published on 24 April 2026. Downloaded on 6/4/2026 6:31:48 PM.
This article is licensed under a Creative Commons Attribution-NonCommercial 3.0 Unported Licence.

also used to ensure that every cathode had the same amount of slurry casted, which was then confirmed when calculating mas loading.

Coin cell assembly

CR2032 coin cells were assembled in an aqueous configuration. The cathodes (14 mm diameter) were placed at the base of the cell case. A 19 mm separator was positioned above, followed by 150 μL of 3 M $Zn(CF_3SO_3)_2$ aqueous electrolyte (applied in 3 × 50 μL increments). A 14 mm Zn foil anode was placed on the separator, followed by a 1 mm spacer and a spring. The cell was sealed by crimping at 750 psi using a manual hydraulic crimper.

Electrochemical tests

Assembled cells were rested for 10 hours before testing. Cyclic voltammetry (CV) was performed in the 0.2–1.6 V range at scan rates from 0.1 to 1 mV s^{-1} using a Biologic MPG-2 system. Galvanostatic charge–discharge (GCD) tests were performed at specific currents of 100, 200, 500, 1000, 2000, 5000, and 10 000 mA g^{-1}. Rate performance and long-term cycling were evaluated at 1000 and 2000 mA g^{-1} using a Neware battery tester. When calculating the specific capacity, the mass of the active material (VO_2(B)) was considered. Electrochemical impedance spectroscopy (EIS) was carried out after 5 and 1000 cycles over a 10 mHz to 100 kHz frequency range with a 10 mV amplitude.

Results and discussion

Fig. 1a presents a schematic illustration of VO_2(B) cathodes integrated with various CCs. Fig. 1b displays the corresponding costs of these CCs in GBP per cm^2, highlighting an important parameter in selecting a suitable CC – particularly as the cost directly influences the overall cost per kWh of energy (note: prices were calculated based on web sources). Additionally, a comparison of material densities is included, which is crucial when considering weight-sensitive applications. From this figure, it can be seen that the stainless-steel materials have the lowest cost, which coupled with the material's good corrosion resistance (see further) and high mechanical strength,[34] make the material a good option for larger scale production. Fig. 1c–h present SEM images of the pristine current collectors and the same substrates after coating with the VO_2(B)-based slurry, including both top-view and cross-sectional perspectives. The top-view SEM images confirm that the nanorod morphology of VO_2(B) is preserved during slurry preparation and casting (consistent with pristine VO_2(B) shown in Fig. S1). The cross-sectional SEM insets reveal differences in interfacial bonding between the CC and the active material.

In the cases of carbon paper (Fig. 1c) and stainless-steel mesh (Fig. 1h), the active material infiltrates and fills the voids of the CC, resulting in no distinct interface – indicative of strong adhesion and integration. This can be attributed to their higher porosity, as evident from the top-view SEMs. In contrast, the remaining CCs exhibit a clear interfacial boundary between the electrode layer and the substrate, suggesting weaker infiltration and limited interfacial contact. Supporting structural and morphological characterisation of VO_2(B), including SEM, XRD, and Raman spectroscopy are provided in the SI (Fig. S1).[35] Understanding the structure of the current collectors is crucial in selecting the best option for your electrode. In this study, VO_2(B) is the active material, which is formed *via* hydrothermal synthesis (SI). Fig. S1 displays the Raman and XRD spectra of the material, ensuring the correct oxide and phase was synthesised, alongside the SEM image of the nanorods formed, for further confirmation. The data obtained show the standard Raman peaks were present, in addition to the expected XRD peaks displayed, confirming that VO_2(B) was formed.[35]

To evaluate the chemical stability of pristine CC materials in the electrolyte environment, each CC (cut into 30 × 10 mm pieces) was submerged in 3 M $Zn(CF_3SO_3)_2$ aqueous electrolyte for 7 days. Prior to immersion, XRD and SEM analyses were conducted for each CC, and repeated after the 7-day submersion. Fig. 2a and b display the comparative XRD spectra. Both stainless steel foil and mesh exhibit no discernible changes in diffraction patterns after electrolyte exposure, indicating excellent structural and chemical stability with no signs of decomposition or degradation. Graphene paper and carbon paper retained their characteristic peak near 25°, though the minor peak around 55° was reduced in graphene paper and completely disappeared in carbon paper – suggesting some minor structural or surface changes. Titanium foil displayed slight peak shifts with enhanced intensity, particularly in the third diffraction peak, indicating crystallinity changes, though the primary structure remained intact. In contrast, CNT paper showed the most significant alteration in XRD patterns: peaks became sharper, the peak at ~44° disappeared, and new peaks emerged at ~20° and ~30°. This could point to the formation of new crystalline phases due to interaction with the electrolyte or residual salt by-products remaining on the surface. Fig. S2 provides the XRD spectra of pure $Zn(CF_3SO_3)_2$, which exhibits no peaks near 20° or 30°. Therefore, CNT paper demonstrates the highest degree of structural change and interaction with the electrolyte among the tested CCs. Fig. 2c–h show SEM images of the CCs before and after 7 days of immersion in the electrolyte, with emphasis on regions exposed to the electrolyte in the post-immersion images. Carbon paper and stainless-steel mesh display visible electrolyte remnants within their structural voids, which is expected due to their relatively large pore sizes. Graphene paper and CNT paper exhibit smaller amounts of electrolyte residue, likely occupying the fine pores between the carbon fibres. In contrast, both titanium and stainless-steel foils show more extensive surface deposition. The presence of surface residues across all materials suggests electrolyte salt precipitation during the immersion period, resulting in visible salt deposits on the current collectors.

Open-circuit voltage (OCV) measurements were conducted on the pristine current collectors to assess their electrochemical stability in the electrolyte without the influence of an applied current. Each CC sample was submerged in 3 M $Zn(CF_3SO_3)_2$ electrolyte for 24 hours and used as the working electrode in a three-electrode setup, with platinum as the counter electrode

Open Access Article. Published on 24 April 2026. Downloaded on 6/4/2026 6:31:48 PM.
This article is licensed under a Creative Commons Attribution-NonCommercial 3.0 Unported Licence.

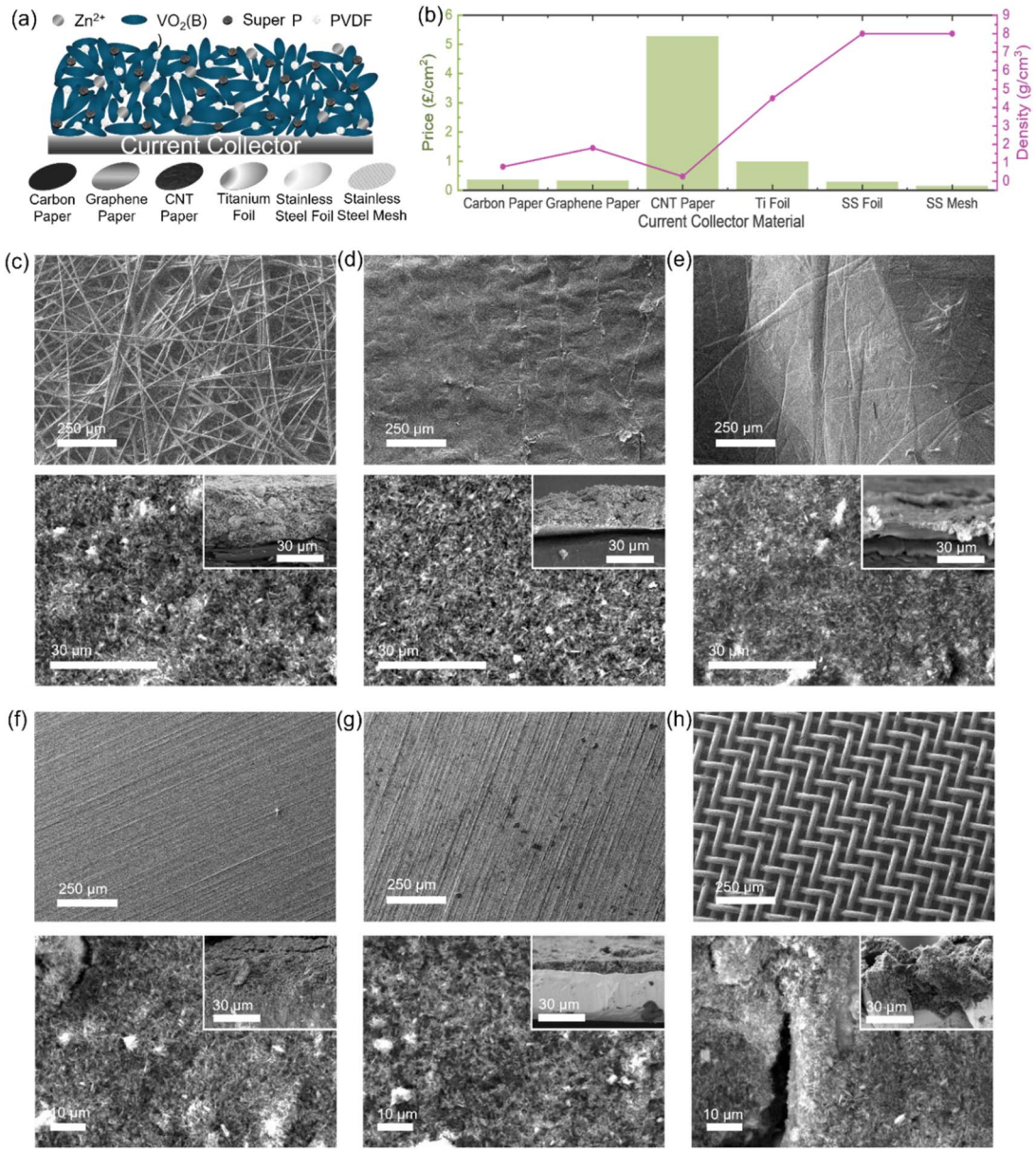

Fig. 1 (a) Schematic illustration of the cathode configuration with various CC materials. (b) Comparative chart showing the cost per cm^2 (in GBP) and density of each CC material. (c–h) SEM images of pristine CCs (top) and corresponding top views of the VO_2(B) slurry-casted electrodes with inset cross-sectional images: (c) carbon paper, (d) graphene paper, (e) CNT paper, (f) titanium foil, (g) stainless steel foil, and (h) stainless steel mesh.

and Ag/AgCl as the reference electrode. Fig. S3a presents the OCV of each CC as a function of time. Among the materials tested, the metal-based current collectors (titanium, stainless steel foil, and mesh) demonstrated the highest voltage stability, with minimal fluctuation following an initial stabilisation phase. This initial drift is attributed to the relaxation of internal electrochemical processes, after which the system approaches thermodynamic equilibrium. Graphene paper exhibited minor voltage fluctuations at approximately 8 and 14 hours, while CNT paper showed a more pronounced delay in reaching a stable OCV, with a noticeable fluctuation around 15 hours. The prolonged stabilisation period of the CNT paper may suggest higher internal resistance or surface reactivity. In contrast, carbon paper displayed excellent stability, with a brief activation period and minimal variation in voltage over time. Fig. S3b–g show high-magnification SEM images of the CC surfaces before and after the OCV tests. These images are consistent with the trends observed in Fig. 2c–h, but at increased magnification, the precipitation and decomposition of electrolyte residues are more clearly visible on the CC surfaces.

Tafel corrosion tests were conducted to determine corrosion rates and mechanisms by measuring the current response of the different current collector materials to polarisation; a three

 This journal is © The Royal Society of Chemistry 2026

Open Access Article. Published on 24 April 2026. Downloaded on 6/4/2026 6:31:48 PM.
This article is licensed under a Creative Commons Attribution-NonCommercial 3.0 Unported Licence.

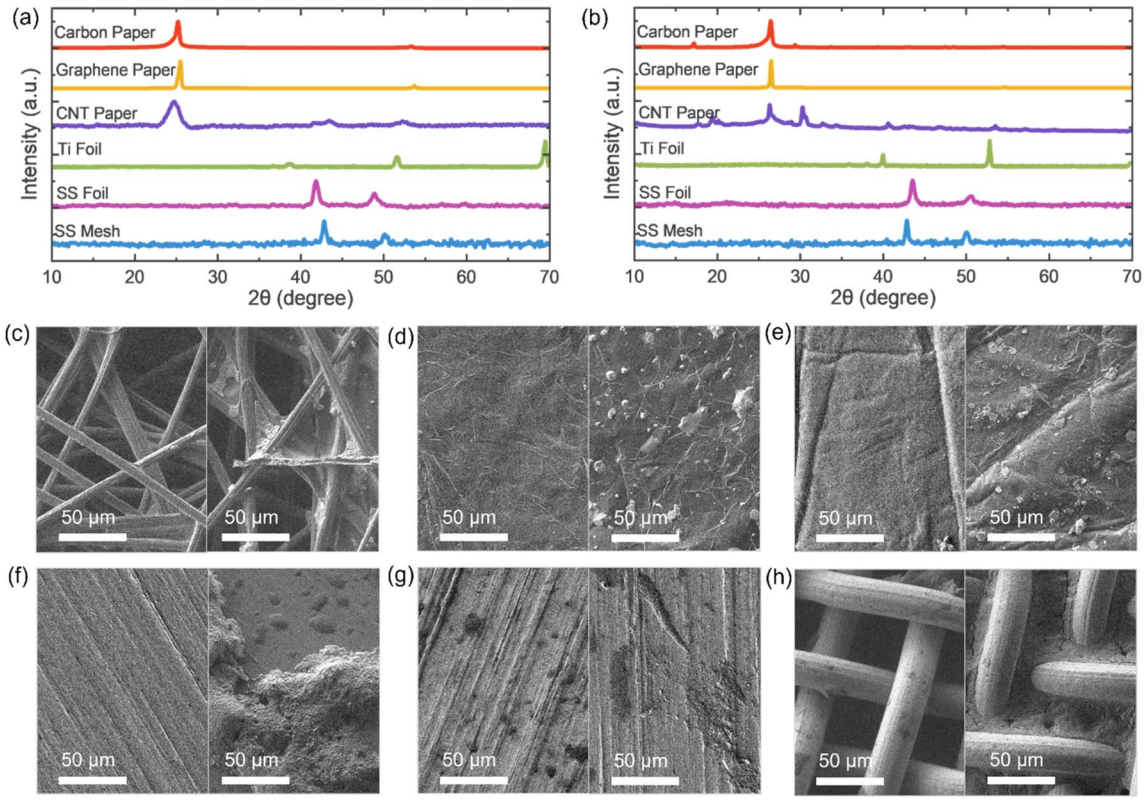

Fig. 2 (a) XRD profiles of current collectors before immersion and (b) after 7 days of immersion in 3 M $Zn(CF_3SO_3)_2$ electrolyte. (c–h) SEM images of pristine (left) and post-immersion (right) current collectors: (c) carbon paper, (d) graphene paper, (e) CNT paper, (f) titanium foil, (g) stainless steel foil, and (h) stainless steel mesh.

electrode system was constructed with the current collector material as the working electrode, zinc foil as the counter electrode and Ag/AgCl as the reference, in 3 M $Zn(CF_3SO_3)_2$, with all foils 30 × 10 mm and current collectors in a 14 mm diameter circle. OCV was held for 30 min, allowing equilibration, then a potential sweep of ±250 mV *vs.* OCV. The i_{corr} of each material is displayed in Fig. 3a, in which carbon paper yields the lowest current density translating to a lower corrosion rate, making it the most stable current collector. Whereas CNT paper has the highest current by far, being at least 30× higher than the rest, rendering it the least corrosion resistance and indicating orders-of-magnitude faster corrosion, greater long-term thickness loss, and a much higher risk of stability and contamination issues under the same conditions. The E_{corr} values are also displayed, showing CNT paper and Ti foil have the lowest E_{corr}, so they are the most thermodynamically prone to start corroding, whereas carbon paper, SS mesh and SS foil sit at more noble potentials and are less easily driven into active dissolution at OCP, even though their i_{corr} values are similar.

Considering both i_{corr} and E_{corr}, carbon paper exhibits the most favourable overall corrosion behaviour among the investigated current collectors. Its corrosion current density (1.71×10^{-8} A cm^{-2}) is the lowest within the group of metallic and carbonaceous substrates that show similarly low i_{corr} values, indicating the slowest uniform dissolution rate at the metal/electrolyte interface. At the same time, carbon paper possesses a relatively noble E_{corr} (0.317 V), comparable to or slightly more positive than those of SS mesh and SS foil, which reflects a reduced thermodynamic driving force for spontaneous anodic dissolution compared with more active materials such as CNT paper and Ti foil. CNT paper, by contrast, combines a markedly higher i_{corr} (3.21×10^{-6} A cm^{-2}) with a more negative E_{corr} (0.089 V), consistent with a kinetically and thermodynamically less stable surface prone to accelerated corrosion under identical conditions. Ti foil displays an intermediate behaviour, with a low i_{corr} but a more active E_{corr}, suggesting good kinetic resistance but a higher driving force for initiation of corrosion. Taken together, the conjunction of very low i_{corr} and a comparatively noble E_{corr} indicates that carbon paper has the lowest overall corrosion susceptibility and is therefore the most promising current collector for long-term operation in the studied electrolyte.

In the full Tafel plots for each material, Fig. 3b–g, relatively significant noise can be observed on the anodic branch of the carbon paper plot; this is prevalent in carbon-based materials due to their heterogeneous surface structure, including defects, and functional groups that oxidise at different potentials. This leads to non-uniform activation of reaction sites as the potential increases. Additionally, surface reactions, restructuring, and possible gas evolution can dynamically change the active area, causing fluctuations in current and resulting in a noisy anodic response. However, graphene paper doesn't exhibit this noise (while CNT paper displays negligible noise); it behaves as a relatively dense, continuous film with uniform conductivity

Open Access Article. Published on 24 April 2026. Downloaded on 6/4/2026 6:31:48 PM.
This article is licensed under a Creative Commons Attribution-NonCommercial 3.0 Unported Licence.

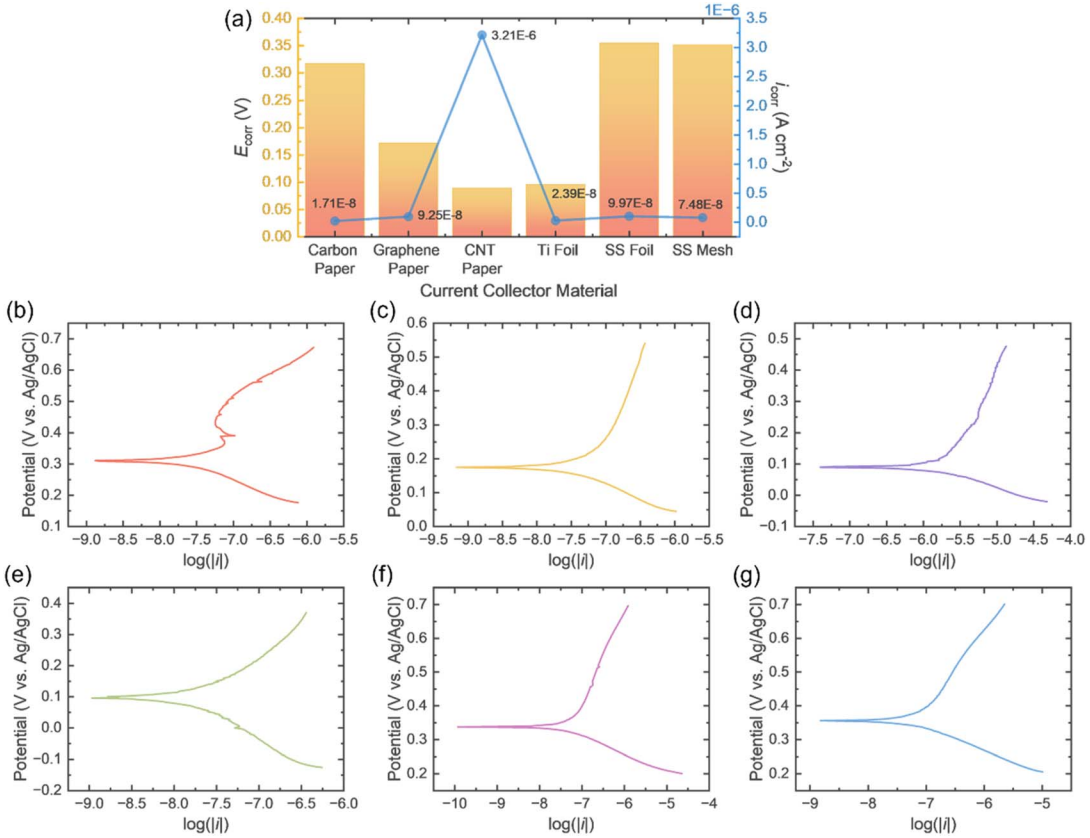

Fig. 3 (a) Comparative chart of i_{corr} and E_{corr} and the polarisation resistance of each current collector material. Tafel plots for different current collector materials; (b) carbon paper, (c) graphene paper, (d) CNT paper, (e) titanium foil, (f) stainless steel foil and (g) stainless steel mesh.

and stable active sites, leading to a consistent current response under anodic polarisation. The faster, more uniform electron transfer and lower interfacial resistance, results in the overpotential/log i relationship being dominated by well-behaved charge-transfer kinetics rather than ohmic and mass-transport artefacts. In contrast, carbon paper has a porous, heterogeneous fibre network with varying surface functional groups, uneven wetting, and distributed reaction sites. During anodic polarisation, this leads to non-uniform activation, surface oxidation, and microbubble formation, causing current fluctuations and a noisy Tafel response. Its lower through-plane conductivity also promotes local iR drops and uneven current distribution, further roughening the anodic branch signal.

After conducting preliminary tests on the CCs alone, electrochemical evaluations were performed to assess their performance within ZIB coin cells and to understand their influence on overall cell behaviour. Initial cyclic voltammetry (CV) measurements were carried out at scan rates ranging from 0.2 to 1.0 mV s^{-1}. Fig. 4a presents the CV profiles of cells with various CC materials at 0.5 mV s^{-1}, while Fig. 4b shows the curves at 1.0 mV s^{-1} (complete CV profiles are available in Fig. S4). Among the tested materials, cells utilising carbon paper and graphene paper as CCs exhibited the best electrochemical behaviour, characterised by two well-defined anodic and cathodic peaks – indicative of fast, reversible redox processes and high electrode kinetics, supported by favourable structural and electrochemical attributes. In contrast SS mesh also displayed two well defined redox peaks, however some noise was exhibited in one of the cathodic peaks and CNT paper produced broader peaks. This may be a result of concentration overpotential, in which reactant depletion near the electrode reduces current amplitude and broadens peaks. That coupled with slight peak shifting, suggesting slower redox kinetics, deems these materials not optimal. The poorest performance was observed in cells with SS and titanium foils, both showing significant signal noise, which points to poor interfacial compatibility and electrochemical instability. The peaks are also shifted; this could be due to overpotential.[36] Slow electron transfer leads to a delayed reaction thus shift the oxidation peaks positively, away from the theoretical voltage, and negatively for the reduction peaks. The plots are distorted and hysteresis is observed, which resistance overpotential could be the cause of, suggesting slow kinetics, overpotential and structural changes (as the curve is asymmetric). This implies that the foils exhibit sluggish kinetics and thus are not favourable.

The pairs of peaks observed in the CV plots are due to the change in valence of the vanadium during the process; as the cell is discharged the zinc anode oxidises and dissolves into the electrolyte as Zn^{2+} ions, while Zn^{2+} ions inserted (intercalated) into the VO_2(B) tunnel like structure. This reduces the VO_2(B) from V^{4+} to V^{3+}, which corresponds to the first peak observed, and again from V^{3+} to V^{2+} which corresponds to the second peak

 This journal is © The Royal Society of Chemistry 2026

Open Access Article. Published on 24 April 2026. Downloaded on 6/4/2026 6:31:48 PM.
This article is licensed under a Creative Commons Attribution-NonCommercial 3.0 Unported Licence.

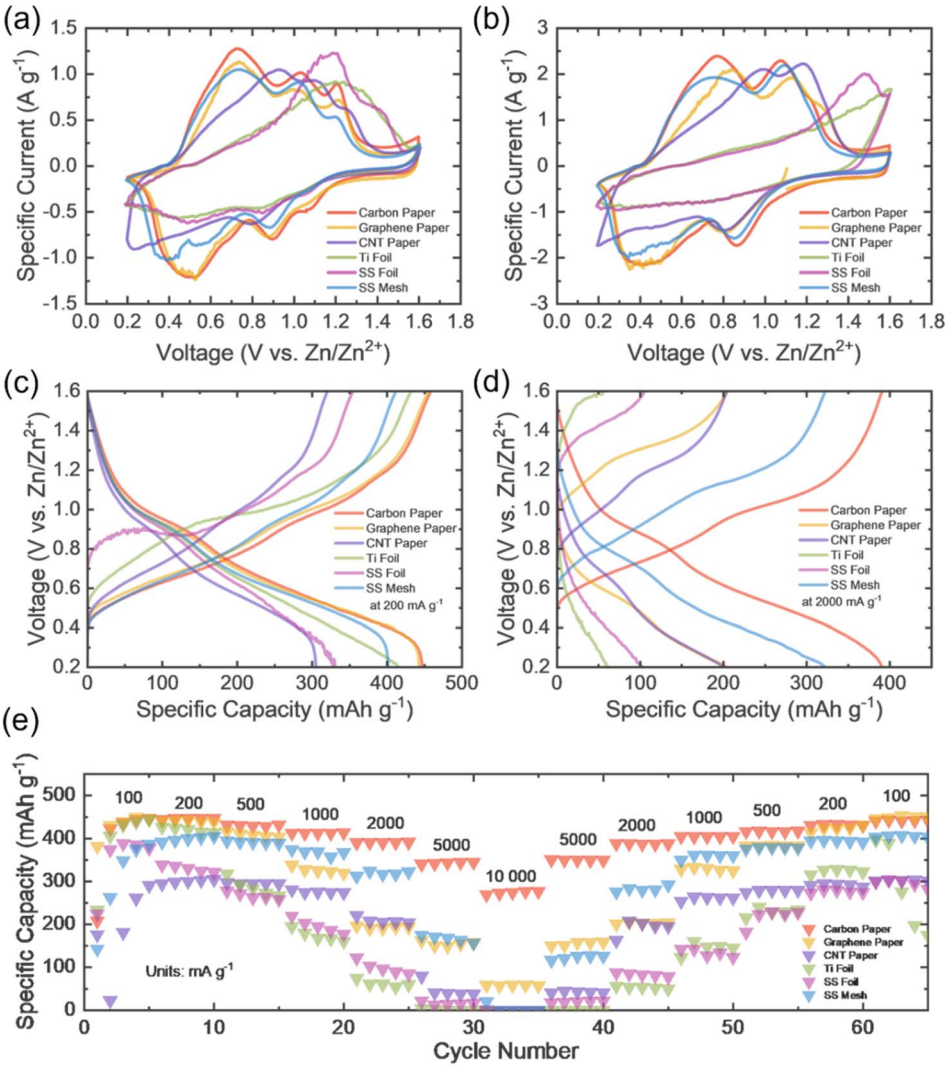

Fig. 4 Comparative CV curves of ZIBs with different current collectors at a scan rate of (a) 0.5 mV s^{-1} and (b) 1.0 mV s^{-1}. Comparative GCD curves of ZIBs with different current collectors at a specific current of (c) 200 mA g^{-1} and (d) 2000 mA g^{-1} and (e) rate tests comparison plot.

in the pair. On charging, the Zn^{2+} ions are extracted from the VO_2(B) material, thus oxidising it and increasing its valence back to 4+, while the Zn^{2+} platting onto the Zn. The eqn (1) and (2) below describe what is happening at the anode and cathode during discharge, respectively.[37]

$$Zn \rightarrow Zn^{2+} + 2e^- \quad (1)$$

$$VO_2(B) + xZn^{2+} + 2xe^- \rightarrow Zn_xVO_2(B) \quad (2)$$

In Fig. 4a, an additional broadening of the CV area can be observed for the cells, which may be attributed to proton (H^+) insertion. The tunnel-like structure of VO_2(B) facilitates the insertion of H^+ ions during discharge, aided by the presence of water in the electrolyte. These protons may intercalate at potentials distinct from those of Zn^{2+} ions, contributing to a pseudocapacitive response. Similarly, during the charging process, H^+ ions may be extracted from the VO_2(B) lattice at voltages different from Zn^{2+} extraction, further supporting the presence of a dual-ion storage mechanism.[38]

Subsequently, galvanostatic charge–discharge (GCD) tests were conducted across a range of specific currents (100–10 000 mA g^{-1}). Fig. 4c and d illustrate GCD profiles at 200 mA g^{-1} and 2000 mA g^{-1}, respectively, for all CC materials. At the lower specific current of 200 mA g^{-1}, the CNT paper and SS foil cells showed the weakest performance, with specific capacities barely reaching 300 mAh g^{-1}, with the SS foil cell exhibiting noisy voltage profiles – suggesting poor electrochemical stability. The remaining CCs demonstrated smoother and more stable curves. At higher specific current of 2000 mA g^{-1}, cells with metal foil CCs showed a pronounced drop in specific capacity by at least 200 mAh g^{-1}, highlighting their kinetic limitations. SS mesh retained capacity relatively well, but the voltage profiles showed less defined plateaus, indicating less sharp phase transitions. Notably, CNT paper, exhibited significant capacity fading and gradual transitions at higher specific currents, pointing to inferior rate capability. In contrast, graphene paper and carbon paper consistently delivered the best performance, respectively. Carbon paper stood out, offering a higher specific capacity

Open Access Article. Published on 24 April 2026. Downloaded on 6/4/2026 6:31:48 PM. This article is licensed under a Creative Commons Attribution-NonCommercial 3.0 Unported Licence.

(447.3 mAh g^{-1}) at the lower applied current, and dropping by approx. 60 mAh g^{-1} at the higher applied current (390.8 mAh g^{-1}), confirming its superiority as a current collector, consistent with prior conclusions.

Fig. 4e presents the rate performance of ZIBs employing various CC materials, with five cycles conducted at each applied specific current. At low current densities (cycles 2–10), both carbon paper and graphene paper exhibit the highest specific capacities (~440–450 mAh g^{-1}), indicating excellent electronic conductivity and effective electrode utilisation. Titanium foil also demonstrates relatively high initial capacity (~420–440 mAh g^{-1}), while SS mesh and SS foil show comparatively lower values, due to reduced wettability and less favourable charge transfer characteristics. CNT paper exhibits poor initial performance, suggesting limitations in electrolyte infiltration or electrical contact within the electrode architecture. As the current density increases (cycles ~15–35), pronounced differences emerge in rate capability. Carbon paper maintains the highest capacity retention (~270 mAh g^{-1} at 10 000 mA g^{-1}), demonstrating superior tolerance to high-rate operation. In contrast, graphene paper shows a moderate decline (~58 mAh g^{-1} at 10 000 mA g^{-1}), indicative of transport limitations arising from its comparatively lower porosity. SS mesh initially retains moderate capacity but undergoes near-complete capacity collapse at the highest rates, attributed to non-uniform current distribution and possible surface passivation, which is also exhibited by SS foil, titanium foil and CNT paper. These results suggest that dense, non-porous current collectors are highly susceptible to transport limitations and interfacial resistance buildup, with titanium foil further affected by the formation of a passive oxide layer that severely impedes charge transfer. Upon returning to low current densities (cycles ~45–65), recovery behaviour provides insight into the reversibility and stability of each system; graphene paper achieves the highest capacity recovery (~450 mAh g^{-1}), closely followed by carbon paper (~440 mAh g^{-1}), indicating minimal irreversible degradation and stable electrode/electrolyte interfaces. SS mesh and CNT paper also demonstrates good recovery (~400 mAh g^{-1} and ~303 mAh g^{-1}), though the cycles are not as uniform as that of graphene and carbon paper, and at the highest applied current capacity is near zero. In contrast, SS foil exhibits only partial recovery, suggesting irreversible structural or interfacial degradation, while titanium foil displays unstable recovery behaviour, with partial capacity restoration followed by subsequent decline, consistent with persistent passivation effects, resulting in cell degradation in the last 3 cycles.

Overall, the results highlight that porous, carbon-based current collectors (excluding CNT paper) significantly outperform metallic counterparts in ZIB systems, owing to enhanced electrolyte accessibility, improved charge distribution, and reduced susceptibility to passivation. While metallic current collectors may offer adequate performance at low rates, their poor high-rate capability and limited reversibility underscore critical limitations for practical applications. Furthermore, due to the medium mass loading of the cathode material on the current collectors, an activation period is seen during the first few cycles which is attributed to progressive electrolyte wetting and improved electrochemical accessibility of the cathode due to the moderate mass loading. In moderately loaded electrodes, portions of the active material are initially poorly wetted or electronically/ionically isolated, leading to underutilisation. With repeated cycling, electrolyte penetration improves, interfacial contact between the active material and current collector becomes more effective, and internal resistance decreases.

Long term galvanostatic cycling of the cells with different CC materials was conducted, to observe the longevity of the current collector and the cell itself. The cells were cycled for 1000 cycles at an applied specific current of 2000 mA g^{-1}, after resting for 10 hours; each cell exhibits an initial activation period before declining into a plateau, therefore the capacity retention was calculated from the highest capacity obtained, *i.e.* after the activation period. CNT current collector cells performed the poorest, failing after ~400 cycles. This could be attributed to progressive interfacial and structural degradation; repeated charge/discharge induces loss of electrical contact between the CNT network and the active material as binder redistribution and microstructural rearrangement occur, increasing internal resistance. Furthermore, side reactions such as electrolyte decomposition and surface oxidation of the carbon scaffold can further reduce conductivity and wettability stability. Stainless steel mesh cells also displayed instability, exhibiting drops and jumps, indicating evolving interfacial contact and non-uniform current distribution; moreover, trapping and release of dead zinc or reversible reactivation of previously isolated active regions can produce step-like recovery behaviour. Though these jumps are present, the SS mesh cell still retained 93% of its capacity (Table S1), outperforming its foil counterpart, which retained only 23%, but displayed a smooth plot after jumps during the first 300 cycles. Titanium foil also displays jumps during cycle; it is common for metals as they undergo dynamic surface conditioning during cycling (formation/removal of oxide layers and adsorbed species), which can temporarily improve or hinder charge-transfer kinetics. Carbon paper yields the highest capacity (226.5 mAh g^{-1} at the 100th cycle), retaining 83.6% of its initial capacity, while graphene paper displays a high initial capacity but only retains 40% of it. Carbon paper is favourable over SS mesh though it retains less of its capacity as it obtains a higher specific capacity and exhibits no jumps/drops, indicated more uniform current distribution.

Note that, the discrepancy between the specific capacity obtained in the GCD rate tests and long term cycling are different due to the kinetics and history; in a rate test the cell is gradually formed at 0.1, 0.2, 0.5 and 1 A g^{-1}, which improves electrolyte wetting, activates sluggish regions, relaxes mechanical strain, and partially optimises the interfacial chemistry before it reaches 2 A g^{-1}, so by then the electrode is in a highly activated state and can utilise more of its thickness even at high current. In contrast, when you start long-term cycling at 2 A g^{-1}, the first few cycles are limited by higher interfacial resistance, incomplete electrolyte penetration and non-uniform current distribution, which increase polarization and make the cell hit the voltage cut-offs earlier, especially in an aqueous ZIB with a relatively narrow potential window.

 This journal is © The Royal Society of Chemistry 2026

Open Access Article. Published on 24 April 2026. Downloaded on 6/4/2026 6:31:48 PM. This article is licensed under a Creative Commons Attribution-NonCommercial 3.0 Unported Licence.

Electrochemical impedance tests were conducted on cells with different current collectors after 5 discharge/charge cycles and 1000 cycles tested at 2000 mA g^{-1}. For each cell, the electrolyte resistance remains relatively similar, none exceeding 10 Ω, and the charge transfer resistance (R_{ct}) increases as the number of cycles do. The R_{ct} values for the cells with foil current collectors were large after 5 cycles (53.82 Ω and 33.83 Ω for titanium and SS foil, respectively) and continued to increase drastically after 2000 cycles (110.54 Ω and 155.24 Ω for titanium and SS foil, respectively). The high resistance is expected, as concluded by the overpotential seen in the CV analysis, and it follows that the resistance should increase after continuous cycling. Cells with stainless steel mesh CC exhibits the next largest increase in R_{ct} as the number of cycles increases, starting from 6.95 Ω and worsening to 11.76 Ω, however the increase is not as drastic as the foils, suggesting that there could be less corrosion and mechanical degradation of the CC material in comparison. Additionally, it also has the lowest resistance (R_{ct}) overall out of all the current collector materials, which could be attributed to the porous mesh structure, allowing efficient electron transport and electrolyte access. The carbon-based materials displayed the least resistance increase as cycling increases; carbon paper cells went from 14.04 Ω to 15.35 Ω, graphene paper increased from 20.68 Ω to 21.83 Ω, and CNT paper resistance grew from 10.80 Ω to 13.68 Ω. This could be owing to the superior corrosion and chemical stability, due to the passivation layer which forms being thinner, more uniform, and chemically stable. Furthermore, carbon-based materials form stable contact with the active material, reducing the potential for poor adhesion during cycling, and their flexibility can better accommodate the volume changes of electrodes during prolonged cycling, without losing contact, whereas metals may suffer from mechanical stresses which increase resistance. The increase in the R_{ct} of the cells after cycling could be due to the fact that continuous cycling consumes active species in the electrolyte, leading to degradation and formation of insoluble by products, as well as side reactions can occur (such as hydrogen evolution), reducing ionic conductivity. Interfacial impedance may occur due to surface contamination and byproduct deposition.

XRD analysis was conducted before and after cycling at 2 A g^{-1} for 2000 cycles (Fig. 5d and e), providing information on how the crystal structure has evolved under electrochemical stress, identifying phase transformations, lattice strains and microstructure changes. All the cathodes show minimal changes in the spectra, with graphene paper displaying the same peak at approx. 52°, however it decreases in intensity, suggesting potential amorphisation. The stainless steel and titanium foils show tiny peaks appearing between 25° and 55°, with titanium foil displaying a negative peak shift (reflecting lattice expansion), and stainless steel mesh shows small peaks appearing between 30° and 65°, though they are so small they are negligible, implying little crystalline by-product formation and more amorphous products. Whereas CNT paper exhibits the generation of three peaks (23°, 25° and 52° approx.), indicating the formation of new phases. Carbon paper displayed the largest change, with several small peaks appearing, which indicates phase change, however its Tafel and electrochemical performance is the best. The strong performance means carbon paper provides excellent conductivity and wettability, so VO_2(B) is very electrochemically active there, but that same high activity and reactive surface chemistry promotes crystallisation of by-products that become XRD-visible over time; carbon paper may drive more pronounced interfacial reactions than the other collectors, resulting in optimal kinetics alongside the formation of more crystalline side products (XRD peaks).

Fig. 5f–k display the SEM images of the cathode after 1000 cycles, including the top view and cross section; from which it can be seen that there is contamination of other molecules, including the electrolyte and the separator used in the cell. VO_2(B) may undergo phase changes, reducing their ability to accept and release the ions efficiently – comparing Fig. 1c–h to 5f–k, slight changes in the morphology can be seen; the VO_2(B) nanorods are less visible after cycling. The Nyquist plots clearly show the carbon-based CCs and the SS mesh to have low electrolyte, charge transfer, and diffusion resistance in comparison to the foils. The overall resistance of the cells with these CCs can also be seen to increase slightly as the number of cycles is increased, as expected. The two cells with the foils as the current collector display a high internal resistance after 5 cycles, which is increased drastically after 2000 cycles, which is not a trend exhibited by the other CCs. It can be stated that SS mesh displays the lowest resistance, followed by carbon and graphene paper, but due to SS mesh's performance during other tests, it is not an overall optimal material, and graphene and carbon paper will be considered as their low R_{ct} facilitates enhanced electrochemical behaviour.[39–41]

Overall, it can be concluded that the general, optimal current collectors are carbon and graphene paper, for most applications. From the long-term cycling (Fig. 5a and b) and rate tests (Fig. 4e), carbon paper has the best capacity retention and rate capabilities, indicating superior charge transfer and lower resistance at the interface. The long-term cycling tests also highlight that the metallic current collectors display capacity fading, which relates to the corrosion and dissolution of the metal; whereas carbon-based materials are chemically inert, though CNT paper doesn't fit this trend due to its structural lacking. Carbon paper's stable capacity also indicated the efficient Zn^{2+} transport across the electrode and interface, attributed to the porosity and durability of the materials, which also benefits adhesion between the current collector ad electrode material. Whereas with rigid foils, interfacial gaps can form during cycling (Fig. 5h–j). Lastly, the low impedance (Fig. 5c and d) and high reversibility (Fig. 4e) indicate a stable interfacial layer, which only slightly forms in ZIBs, following the expected trend of metals forming thicker ones.

Li *et al.* published a literature review of all the different types of current collectors for zinc ion batteries, but did not conduct the tests themselves (making this review of higher novelty and credibility), in which they came to the same conclusion; that overall the carbon based materials yielded higher capacities when compared to the metal current collectors.[42] Ni *et al.* also released a literature review on current collector materials and came to the same conclusion; that carbonaceous materials are

Open Access Article. Published on 24 April 2026. Downloaded on 6/4/2026 6:31:48 PM.
This article is licensed under a Creative Commons Attribution-NonCommercial 3.0 Unported Licence.

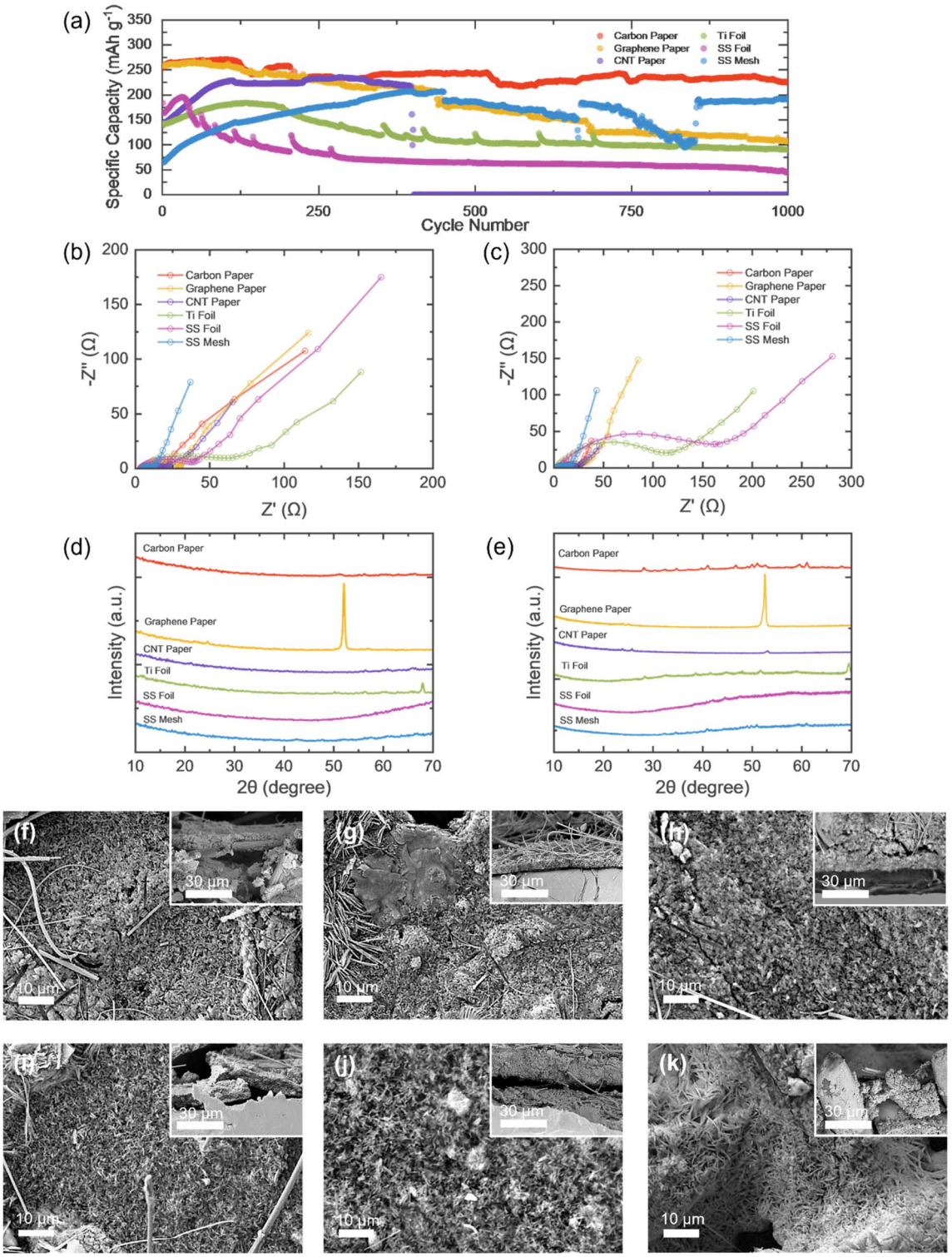

Fig. 5 (a) Comparative long-term cycling plots of ZIBs with different current collectors, at 2000 mA g^{-1}. Comparative Nyquist plots of ZIBs after (b) 5 and (c) 2000 cycles, at 2 A g^{-1}. Comparative XRD profiles of cathodes with different current collectors (d) before and (e) after cycling at 2 A g^{-1} for 2000 cycles. SEM images of the cathode surface after long-term cycling at 2 A g^{-1} for different current collector materials; (f) carbon paper, (g) graphene paper, (h) CNT paper, (i) titanium foil, (j) stainless steel foil and (k) stainless steel mesh. Insets show cross-sectional views of the cycled cathodes.

used due to their high electrical conductivity, good corrosion resistance and the porous nature allowing more mass loading of active materials than foil-type metal current collectors.[43] Other publications have been released comparing a few materials for current collectors for ZIBs, such as Zhang *et al.*,[44] compared a range of metal foils as current collectors for ZIBs with MnO_2

 This journal is © The Royal Society of Chemistry 2026

Open Access Article. Published on 24 April 2026. Downloaded on 6/4/2026 6:31:48 PM.
This article is licensed under a Creative Commons Attribution-NonCommercial 3.0 Unported Licence.

based cathodes. Mittal and Kundu produced a review investigating similar current collector materials as in this review,[45] but they focussed on the electrochemical stability of the materials, namely corrosion tests, in a 3-electrode cell system. Thus, this work offers a comprehensive analysis of the various current collectors employed in ZIBs, with particular emphasis on their electrochemical performance, corrosion behaviour, and interfacial binding with the active cathode material.

Conclusion

This study systematically investigated the characteristics and electrochemical performance of various current collector materials for ZIBs using a combination of structural, corrosive and electrochemical analysis. Among the tested materials, carbon paper demonstrated the most promising performance, delivering high specific capacities of 447.5 mAh g^{-1}, respectively, with excellent capacity retention of 83.6% after 1000 cycles at 2000 mA g^{-1}. The material also exhibited improved rate capability and cycling stability, confirming its robustness as a current collector. Additionally, carbon paper obtained the lowest i_{corr} (1.71×10^{-8} A cm^{-2}), making it the material with the slowest uniform dissolution rate, while possessing a noble E_{corr} (0.317 V), reflecting a lowered thermodynamic driving force for spontaneous anodic dissolution; though it did change the most noticeably when analysed *via* XRD before and after cycling, however this did not have a significant effect on the electrochemical performance of the cell so was negligible. While the choice of current collector ultimately depends on the intended application of the ZIB, this work identifies carbon paper as the optimal material for ZIBs employing VO_2(B) cathodes. Their low cost and density, chemical stability in aqueous electrolytes, enhanced electrochemical performance, long-term cycling durability, and low internal resistance make them highly suitable candidates for scalable and reliable ZIB applications.

Conflicts of interest

The authors declare no competing financial interest.

Data availability

The raw data supporting the findings of this study are available from the corresponding authors upon reasonable request.

Supplementary information (SI): SEM, Raman, and XRD characterization of VO_2(B) cathode nanorods; separator and electrolyte structural analysis; OCV stability studies of different current collectors; cyclic voltammetry comparison of six current collector materials; and long-term cycling performance with capacity retention data after 1000 cycles for aqueous Zn-ion batteries. See DOI: https://doi.org/10.1039/d5ta07993d.

Acknowledgements

B. D. B. acknowledges support from the EPSRC research grant EP/Y008103/1 and EP/U536830/1.

References

1 L. P. He, S. Y. Sun, X. F. Song and J. G. Yu, *Waste Manage.*, 2015, **46**, 523–528.
2 L. Ma, X. Wang and J. Sun, *J. Electroanal. Chem.*, 2020, **873**, 114395.
3 D. Kundu, B. D. Adams, V. Duffort, S. H. Vajargah and L. F. Nazar, *Nat. Energy*, 2016, **1**(10), 1–8.
4 R. Zhu, Z. Xiong, H. Yang, N. Wang, S. Kitano, C. Zhu, Y. Aoki, H. Habazaki, R. Zhu, Z. Xiong, H. Yang, N. Wang, S. Kitano, Y. Aoki, H. Habazaki and C. Zhu, *Adv. Funct. Mater.*, 2023, **33**, 2211274.
5 N. Zhang, X. Chen, M. Yu, Z. Niu, F. Cheng and J. Chen, *Chem. Soc. Rev.*, 2020, **49**, 4203–4219.
6 R. Tang, Y. Feng, Y. Liu, Y. Wu, Q. Liu, G. Hu and X. Liu, *Chem. Eng. J.*, 2025, **523**, 168559.
7 G. Lu, D. Qin, Y. Huang, J. Ding, L. Zhuo, Y. Feng and X. Liu, *J. Energy Storage*, 2025, **137**, 118696.
8 B. Tang, L. Shan, S. Liang and J. Zhou, *Energy Environ. Sci.*, 2019, **12**, 3288–3304.
9 L. Chen, Q. An and L. Mai, *Adv. Mater. Interfaces*, 2019, **6**, 1900387.
10 T. Zhou, L. Zhu, L. Xie, Q. Han, X. Yang, L. Chen, G. Wang and X. Cao, *J. Colloid Interface Sci.*, 2022, **605**, 828–850.
11 T. R. Juran, J. Young and M. Smeu, *J. Phys. Chem. C*, 2018, **122**, 8788–8795.
12 C. Li, X. Zhang, W. He, G. Xu and R. Sun, *J. Power Sources*, 2020, **449**, 227596.
13 M. Song, H. Tan, D. Chao, H. Jin Fan, M. Song, H. Tan, D. Chao and H. J. Fan, *Adv. Funct. Mater.*, 2018, **28**, 1802564.
14 T. Wei, Q. Li, G. Yang and C. Wang, *J. Mater. Chem. A*, 2018, **6**, 8006–8012.
15 B. Tang, J. Zhou, G. Fang, S. Guo, X. Guo, L. Shan, Y. Tang and S. Liang, *J. Electrochem. Soc.*, 2019, **166**, A480–A486.
16 W. Deng, C. Li, W. Zou, Y. Xu, Y. Chen and R. Li, *Small*, 2024, **20**, 2309527.
17 J. R. Loh, J. Xue and W. S. V. Lee, *Small Methods*, 2023, **7**, 2300101.
18 T. Zhang, Y. Tang, S. Guo, X. Cao, A. Pan, G. Fang, J. Zhou and S. Liang, *Energy Environ. Sci.*, 2020, **13**, 4625–4665.
19 G. Li, L. Sun, S. Zhang, C. Zhang, H. Jin, K. Davey, G. Liang, S. Liu, J. Mao and Z. Guo, *Adv. Funct. Mater.*, 2024, **34**, 2301291.
20 Y. Zhang, X. Zheng, N. Wang, W. H. Lai, Y. Liu, S. L. Chou, H. K. Liu, S. X. Dou and Y. X. Wang, *Chem. Sci.*, 2022, **13**, 14246–14263.
21 L. Li, S. Jia, Z. Cheng and C. Zhang, *ChemSusChem*, 2023, **16**, e202202330.
22 J. Wan, R. Wang, Z. Liu, L. Zhang, F. Liang, T. Zhou, S. Zhang, L. Zhang, Q. Lu, C. Zhang and Z. Guo, *ACS Nano*, 2023, **17**, 1610–1621.
23 J. Cao, F. Zhao, W. Guan, X. Yang, Q. Zhao, L. Gao, X. Ren, G. Wu and A. Liu, *Small*, 2024, **20**, 2400221.
24 B. Yin, S. Zhang, K. Ke, T. Xiong, Y. Wang, B. K. D. Lim, W. S. V. Lee, Z. Wang and J. Xue, *Nanoscale*, 2019, **11**, 19723–19728.

Open Access Article. Published on 24 April 2026. Downloaded on 6/4/2026 6:31:48 PM.
This article is licensed under a Creative Commons Attribution-NonCommercial 3.0 Unported Licence.

25 N. Jaikrajang, W. Kao-Ian, T. Muramatsu, R. Chanajaree, T. Yonezawa, Z. Y. Al Balushi, S. Kheawhom and R. Cheacharoen, *ACS Appl. Energy Mater.*, 2021, **4**, 7138–7147.
26 P. Zhu, D. Gastol, J. Marshall, R. Sommerville, V. Goodship and E. Kendrick, *J. Power Sources*, 2021, **485**, 229321.
27 H. Li, L. Li, W. Liu, S. Jia, S. Yue, Y. Yang, C. Wang, C. Tan and D. Zhang, *Chem. Rec.*, 2025, **25**, e202400217.
28 X. Hu, B. Narayan, N. Naresh, I. Pinnock, Y. Zhu, X. Liu, T. Wang, B. Li, I. P. Parkin and B. D. Boruah, *Small*, 2024, **20**, 2403555.
29 J. Tang, J. Cao, Y. Jiang, S. Gou, R. Yao, Y. Li and B. T. Liu, *Green Chem.*, 2024, **26**, 7990–7996.
30 J. Luo, M. Cao, N. Naresh, J. Borah, S. Li, T. Wang, B. K. Sarma, J. Yao, I. P. Parkin and B. D. Boruah, *Adv. Funct. Mater.*, 2024, **35**, 2417607.
31 I. P. Pinnock, Y. Fan, Y. Zhu, B. Narayan, T. Wang, I. P. Parkin and B. D. Boruah, *J. Mater. Chem. A*, 2025, **13**, 1372–1383.
32 M. Yamada, T. Watanabe, T. Gunji, J. Wu and F. Matsumoto, *Electrochem*, 2020, **1**, 124–159.
33 J. Ding, Z. Du, L. Gu, B. Li, L. Wang, S. Wang, Y. Gong and S. Yang, *Adv. Mater.*, 2018, **30**, 1800762.
34 H. Heo, J. Lee, Y. R. Jo and G. H. An, *Adv. Energy Mater.*, 2025, **15**, 2500261.
35 I. P. Pinnock, Y. Fan, Y. Zhu, B. Narayan, T. Wang, I. P. Parkin and B. D. Boruah, *J. Mater. Chem. A*, 2025, **13**, 1372–1383.
36 N. Elgrishi, K. J. Rountree, B. D. McCarthy, E. S. Rountree, T. T. Eisenhart and J. L. Dempsey, *J. Chem. Educ.*, 2017, **95**, 197–206.
37 L. Chen, Y. Ruan, G. Zhang, Q. Wei, Y. Jiang, T. Xiong, P. He, W. Yang, M. Yan, Q. An and L. Mai, *Chem. Mater.*, 2019, **31**, 699–706.
38 B. Zhang, J. Chen, W. Sun, Y. Shao, L. Zhang and K. Zhao, *Energies*, 2022, **15**, 4698.
39 J. Zhou, S. Yang, P. Xu, X. Shi, J. Xu, L. Shao, Y. Sun and Z. Sun, *Chem. Commun.*, 2025, **61**, 3339–3342.
40 W. Xiao, S. Yang, R. Jiang, Q. Huang, X. Shi, Y. H. Tsang, L. Shao and Z. Sun, *J. Mater. Chem. A*, 2024, **12**, 5530–5539.
41 Q. Huang, L. Shao, X. Shi, J. Guan, J. Xu, Y. Wu and Z. Sun, *Chem. Eng. J.*, 2023, **468**, 143738.
42 H. Li, L. Li, W. Liu, S. Jia, S. Yue, Y. Yang, C. Wang, C. Tan and D. Zhang, *Chem. Rec.*, 2025, **25**, e202400217.
43 Q. Ni, B. Kim, C. Wu and K. Kang, *Adv. Mater.*, 2022, **34**, 2108206.
44 G. Zhang, W. Zhou, M. Chen, Q. Wang, A. Li, J. Xu and J. Chen, *Electrochim. Acta*, 2023, **437**, 141519.
45 U. Mittal and D. Kundu, *J. Electrochem. Soc.*, 2021, **168**, 090560.

 This journal is © The Royal Society of Chemistry 2026